Generative Feature Extraction From Sentinel 1 and 2 Data for Prediction of Forest Aboveground Biomass in the Italian Alps

Parth Naik, Michele Dalponte, *Senior Member, IEEE*, and Lorenzo Bruzzone, *Fellow, IEEE*

***Abstract*—Aboveground biomass (AGB) is an important forest attribute directly linked to the forest carbon pool. The use of satellite remote sensing (RS) data has increased for AGB prediction due to their large footprint and low-cost availability. However, they have been limited due to saturation effect that leads to low prediction precision. In this article, we propose an innovative and dynamic architecture based on generative neural network that extracts target oriented generative features for predicting forest AGB using satellite RS data. These features are more resilient to mixed forest types and geographical conditions as compared to the traditional features and models. The effectiveness of the proposed features was assessed by experiments performed using multispectral, synthetic aperture radar, and combined dual-source datasets. The proposed model achieved best performance in terms of precision, model agreement, and overfitting as compared to the other conventional models for all analyzed datasets. The t-distributed stochastic neighbor embedding scatterplots of the generative features clearly show one dimension of the feature space associated with the target AGB. Feature importance analysis indicated that the produced generative features were more significant than the conventional analytical features. Also, the model provided a robust framework for homogeneous fusion of multisensor features from satellite RS data for predicting AGB.**

***Index Terms*—Aboveground biomass (AGB), feature extraction, feature fusion, generative features, variational autoencoder.**

I. Introduction

THE extraction of effective features and precise training data from remote sensing (RS) images is crucial for accurately quantifying and mapping various ecological parameters including the carbon stored in forests [1]–[5]. The quality of these extracted features directly affects the response of the modeling algorithm to predict the target parameter [6]–[8]. Conventional features from RS data are primarily based on specific indices derived by analytical formulations (i.e., arithmetic operations performed on spectral bands, radar backscatters, or elevation statistics of lidar point clouds) [9]–[11]. In the literature, these analytical features are frequently used for different applications like analysis of vegetation, crops, and soil properties [12]. Their effectiveness is found to be highly data dependent [13], [14]. Three-dimensional (3-D) airborne lidar data are very effective in modeling forest parameters. Features such as height and intensity percentiles, height bins, and density metrics are used for the prediction of forest aboveground biomass (AGB) with lidar [15]. However, the effectiveness of such analytical features depends on the point density and the footprint of the laser pulse [16], [17]. Moreover, the limited availability of lidar data and the high cost for finer specifications discourages its use in many operational scenarios. In this context, satellite RS data proves to be a more feasible choice for the forest applications.

Studies performed with satellite multispectral (MS) and synthetic aperture radar (SAR) data used vegetation indices (e.g., normalized difference vegetation index (NDVI), soil adjusted vegetation index (SAVI)), vegetation biophysical features (e.g., leaf area index, chlorophyll concentration), textural features (e.g., entropy, variance), and SAR polarimetric indices for the prediction of forest AGB [18]–[20]. A prominent limitation identified with MS data was a high variation in response of the extracted features that depended on the time of acquisition and the spatio-spectral specifications [19], [21]. The main causes of such reduced prediction precision were linked to the seasonal variation of the spectral responses from the forest. Moreover, the radiometric characteristics of different satellite sensors also affects the performance of the models. In [19], it was observed that MS sensors with different radiometric specifications for an identical spectral range produce nonidentical responses. A few other studies that used Sentinel-2, RapidEye, and PlanetScope data on different forest types also indicated such prediction precision problems that can be traced back to variations in spectral responses and radiometric specifications of sensors [34], [35]. Pham *et al.* [22] discussed a series of opportunities and challenges regarding the prediction of forest AGB using various RS data (optical, SAR, hyperspectral, and lidar) for mangrove forests. Despite these identified challenges, a dedicated attention on extracting target-oriented features from satellite MS and SAR data can greatly increase the prediction precision and provide an economical source for forest parameter estimation.

Manuscript received November 25, 2021; revised March 11, 2022 and May 13, 2022; accepted May 23, 2022. Date of publication May 30, 2022; date of current version June 21, 2022. This work was supported by the Highlander project co-financed by the Connecting European Facility Programme of the European Union under Grant Agreement n° INEA/CEF/ICT/A2018/1815462. *(Corresponding author: Parth Naik.)*

Parth Naik is with the Department of Information Engineering and Computer Science, University of Trento, 38123 Trento, Italy (e-mail: parth.naik@unitn.it).

Michele Dalponte is with the Research and Innovation Center, Fondazione Edmund Mach, 38098 San Michele all'Adige, Italy (e-mail: michele.dalponte@fmach.it).

Lorenzo Bruzzone is with the Department of Information Engineering and Computer Science, University of Trento, I-38123 Trento, Italy (e-mail: lorenzo.bruzzone@unitn.it).

Digital Object Identifier 10.1109/JSTARS.2022.3179027

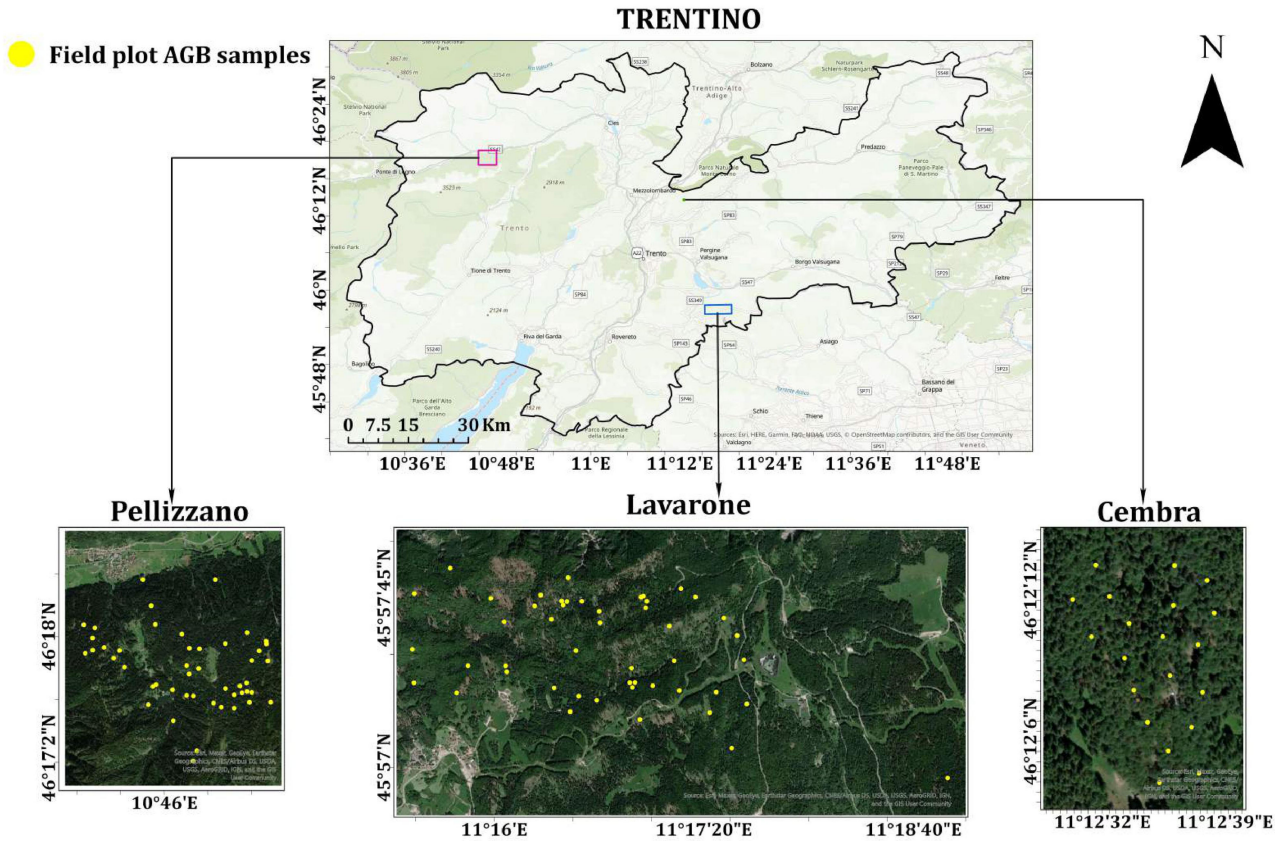

Fig. 1. Location of the three study sites with field plot locations (yellow dots) on Google Earth images.

The ease of access to data is an important aspect for regional and global level mapping of forest AGB [23], [24]. Lidar data are mostly acquired from airborne platforms and are available for only limited geographical locations. Most studies that attempt to map forest AGB on a regional or national scale use satellite remote sensing data that includes SAR and MS data [24]–[27]. SAR can penetrate and gather information from the trunks and branches of the trees which are prime components of AGB [25]. SAR-based studies indicate that long wavelength data (P and L bands) have a higher correlation with AGB [28]–[31]. However, long wavelength open-source SAR data are not available and the cost of commercial SAR data is relatively high. Sentinel-1 satellites provide a huge open-source repository of C-band SAR (short wavelength) data that however are characterized by low penetration into the canopy and features that rapidly saturate for AGB modeling [32], [33]. Different studies have suggested that a synergetic use of SAR and MS data can provide additional features and reduce model saturation caused due to either short wavelength (C-band) or limited spectral channels of the data. This has been particularly observed for Sentinel-1 and Sentinel-2 data [36], [37].

Different machine learning (ML) algorithms (such as random forest (RF), neural networks (NN), and Gaussian processes) have been used in the literature to model forest AGB using various multisensor RS data [41]–[43]. Some of these ML algorithms (e.g., RF, NN, and SVM) have also been used in combination via ensemble learning for further improving AGB prediction

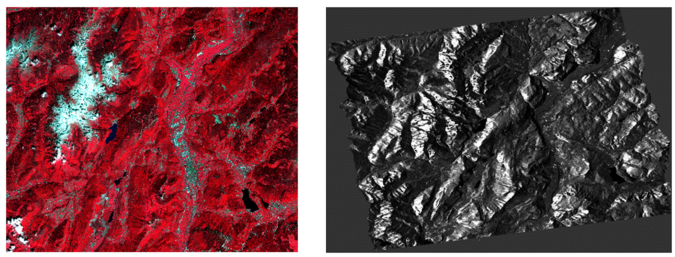

Fig. 2. False color composite of Sentinel-2 (left) and Polarimetric matrix element (C11) of Sentinel-1(right) for the summer season of the study area.

accuracy as compared to single ML algorithms [44], [45]. The recent advances in ML and artificial intelligence have provided different methodologies based on generative and reinforcement learning to extract and engineer data-driven target-oriented features [38]–[40]. Deep neural networks are capable of extracting high level abstract features from complex distribution underlying various RS data [46], [47] by generating an optimal feature space for modeling a given problem. Such abstract features have delivered improved performances in various RS applications [5], [48]–[50]. However, the use of such abstract features for regression problems has been less studied as compared to other applications in the field of RS [51]–[53]. In recent papers, several effective approaches using generative adversarial networks (GAN) and conditional GAN have been developed to learn and productively engineer features from the data [54]–[59],

TABLE I
ACQUISITION DATES (YYY-MM-DD) OF SENTINEL-2 AND SENTINEL-1 IMAGES

Seasons	Dates of Acquisition (YYYY-MM-DD)	
	Sentinel-2	Sentinel-1
Spring	2016-3-10	2016-3-04
Summer	2016-6-28	2016-6-28
Autumn	2016-9-06	2016-9-08
Winter	2016-12-28	2016-12-29

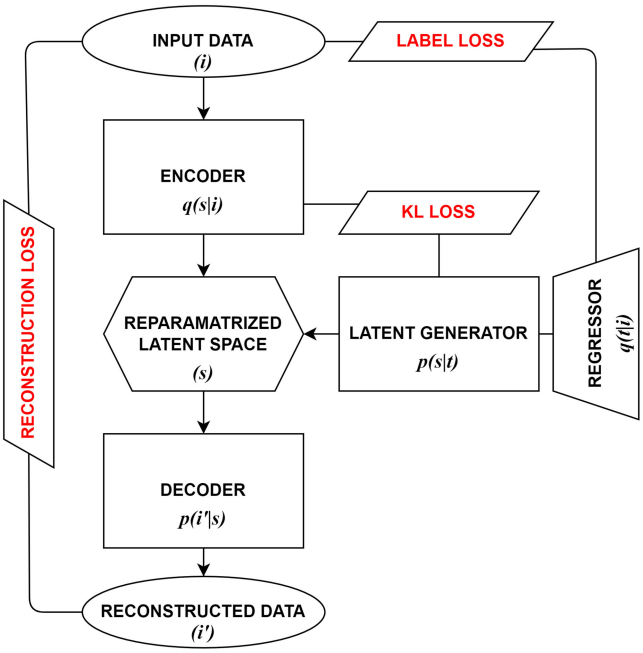

Fig. 3. Framework of the proposed generative model.

[76]. This has led to the use of generative neural networks to effectively disentangle the latent space of the network to explain specific factors of variation in a target variable, thus showing a high potential to solve regression problems [60]–[64]. Unlike traditional approaches that used a conventional multilayer perceptron or stacked sparse autoencoder [65]–[67], a generative neural network can be used to conditionally distribute the feature space on a target variable, consequently improving the accuracy, and generalization of a regression model.

In this article, we consider dual source (MS and SAR) satellite RS data and use advanced generative neural networks for modeling forest AGB. In particular, we propose a dynamic framework based on a generative variational autoencoding to engineer abstract form of target-oriented features. The network aims to generate a highly ordered feature space that can potentially minimize the problem of variability of features for AGB prediction. The network also reduces the input dimensionality to produce a low dimensional feature space reducing the model complexity. The proposed model also adjusts the number of network parameters as per the dimension of the input data to quickly optimize the network and learn effectively. Thus,

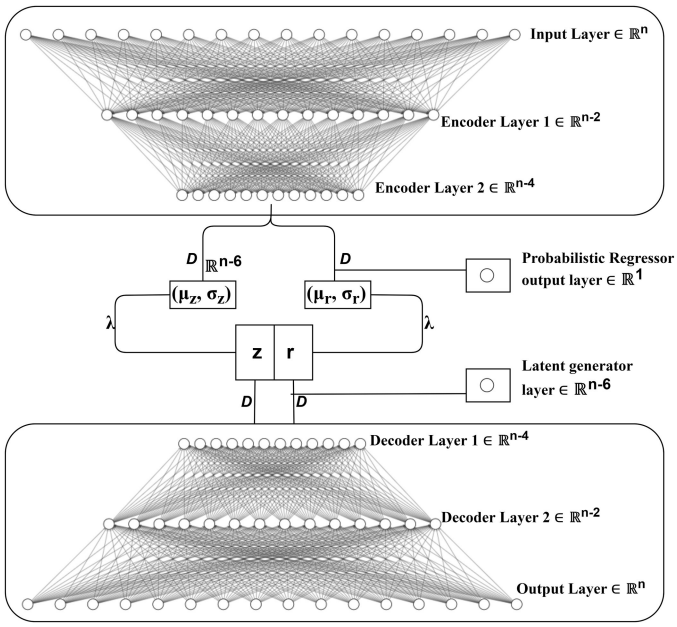

Fig. 4. Dynamic architecture of the proposed generative network. $\mathbb{R}^n$: Network layer of dimension "n"; D: Dense network connection; λ: Reparametrization function; (z, r): Sampled latent vectors; (μ_z, σ_z): Mean and variance of "z"; (μ_r, σ_r): Mean and variance of "r".

we propose an approach that performs target-oriented feature engineering and models AGB using a single dynamic neural network architecture.

II. MATERIALS AND STUDY AREAS

A. Study Area Description and Field Data

The study area consists of three sites,—Lavarone, Pellizzano, and Cembra. These sites are diverse in terms of species/forest type and all are located in the Province of Trento, Italy. The forest in Lavarone consists of coniferous species such as Norway spruce (*Picea abies* (L.) Karst.) and Silver fir (*Abies alba* Mill.) in majority and a minor population of European beech (*Fagus sylvatica* L.), European larch (*Larix decidua* Mill.), and Scots pine (*Pinus sylvestris* L.). The forest in Pellizzano consists of coniferous Norway spruce (*Picea abies* (L.) Karst.) as a dominant species and a trace population of few broadleaves species (*Populus tremula* L., *Betula* spp.). The forest in Cembra mainly consists of broadleaves species such as European beech (*Fagus sylvatica* L.) and few coniferous species. The geographical locations of the study area sites are shown using detailed maps in Fig. 1.

The field data consist of 115 circular plots with fixed radius of 15 m (see Fig. 1). The plots were surveyed in summer 2014 for Pellizzano and summer 2016 for Lavarone and Cembra. A total of 47 plots in Pellizzano, 48 plots in Lavarone, and 20 plots in Cembra were measured using a random sampling design. Coordinates of the plot centers were recorded using a survey-grade GPS unit. In each plot, the diameter at breast height (DBH), height, species and relative positions of all trees having DBH above 7 cm were recorded. The positions were measured

with a Laser criterion 400 and DBH was measured with a caliper in two orthogonal directions and the average among the two measurements was considered as DBH value. The height was measured with a vertex hypsometer and the trees for which the height was difficult to measure, it was estimated using species specific allometric equations [74]. The volume of each tree was estimated using species specific equations [74] with a mean absolute error of 2% for trees with DBH higher than 17 cm. The AGB was obtained by multiplying the volume with species specific conversion factors [75]. Both height and AGB equations were specifically developed for the tree species present in the Autonomous Province of Trento. Appendix A reports the used AGB equations. The plot AGB was obtained by summing the AGB of each tree inside a given plot. The field estimated plot level AGB values ranged from 1.07 Mg ha^{-1} to 655.14 Mg ha^{-1} (1 Mg ha^{-1} = 0.1 kg m^{-2}). In order to test the performance of the proposed model over an independent dataset that was not used in the model training part, we used 55 plots surveyed in 2016 over different sites in the area of the Autonomous Province of Trento. The AGB of these plots used for offsite-validation was in the range of 11.30–711.41 Mg/ha.

B. Remote Sensing Data

This article was performed using multitemporal images acquired by ESA's Sentinel-2 and Sentinel-1 satellite constellations. Four images per satellite constellation were considered, one for each season (see Table I). Sentinel-2 images are characterized by 13 spectral bands of which ten bands were used, i.e., four bands (R, G, B, and NIR) at 10 m spatial resolution and six bands (three Red-Edge, Narrow NIR, and two SWIR) at 20 m spatial resolution. The downloaded data was L1C-level and was acquired from the Planet Labs portal.[1] The Sentinel-2 tiles were acquired with a 10% cap on cloud coverage, although we ensured that the study area covered in each tile and especially the reference plot locations were cloud free for each image. The Sentinel-1 data was acquired from the NASA's Earth Data portal.[2] Level-1 single look complex (SLC) data comprising complex imagery with amplitude and phase captured in the IW mode were used. The resolution of the data (range X azimuth) ranges from (2.7×22 m to 3.5×22 m) and the pixel spacing (range X azimuth) is 2.4×14.1 m with 1×1 number of looks. The acquired SLC product has all bursts in all subswaths and is resampled to a common pixel spacing grid in range and azimuth. The Sentinel-2 and Sentinel-1 images of the study area for the summer season are shown in Fig. 2.

III. Proposed Generative Model Framework and Architecture

A. Generative Model Framework

The proposed generative neural network model adopts a variational autoencoder based modeling framework with a dynamic architecture. A traditional variational autoencoder consists of two main component networks—an encoder and a decoder. The additional two networks added to this traditional architecture are—a latent generator and a regressor network. Unlike traditional approaches that separately trains a feed-forward regressor network, the proposed approach has an integrated regressor network connected to the reparametrized latent space via a latent generator network. All these networks are interassociated with a combination of three loss functions, as shown in Fig. 3.

The probabilistic encoder network ($q(s|i)$) learns the distribution from the input data (i) and generates a reparametrized latent space (s) using a conditional prior of the target parameter (t) instead of a traditional Gaussian prior. The dimension of the input data is compressed by the encoder network to the dimension of the latent space and the latent generator ($p(s|t)$) captures the target specific prior of the latent representations. In this process, the decoder network ($p(i'|s)$) captures the nonlinearity of the latent generator via the generated latent representations and attempts to reconstruct the input. The reconstructed form of the input data is given as (i'). The conjoined feed-forward neural network ($q(t|i)$) is a probabilistic regressor, which predicts outputs along with the bias in prediction (standard deviation).

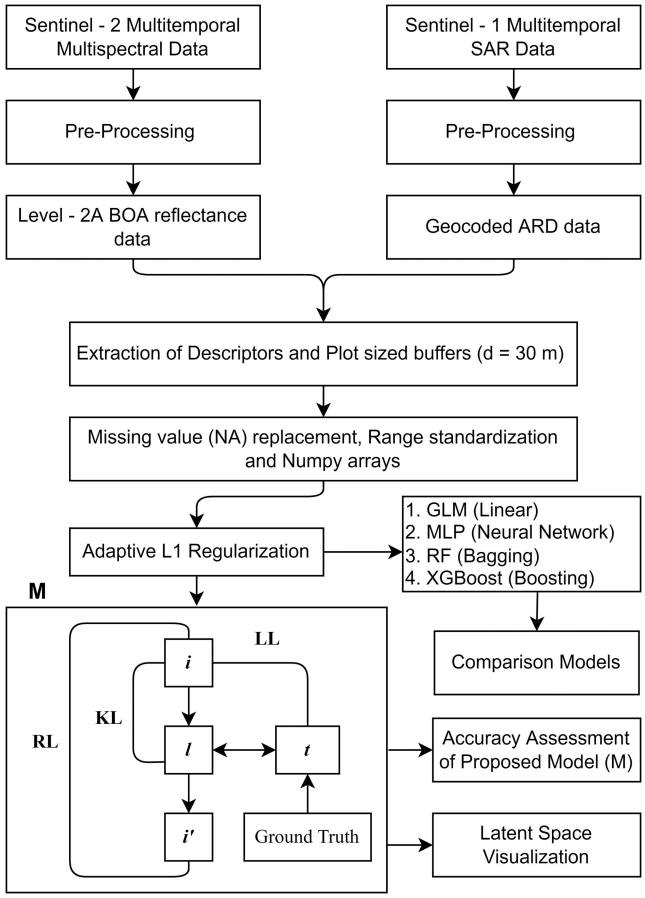

Fig. 5. Flowchart of the proposed approach. BOA: Bottom of atmosphere; ARD: Analysis ready data; GLM: Generalized linear modeling; MLP: Multilayer perceptron regressor; RF: Random forest; XGBoost: Extreme gradient boosting; M: Proposed generative model; i: Input; i': Reconstructed; l: latent space; t: target; RL: Reconstruction loss; KL: KL loss; LL: Label.

[1][Online]. Available: https://www.planet.com/explorer/
[2][Online]. Available: https://urs.earthdata.nasa.gov/

TABLE II
ANALYTICAL FEATURES FROM MS SENTINEL-2 DATA AND THEIR EQUATIONS

Analytical MS Features	Equations
Canopy Chlorophyll Content Index	$\mathrm{CCCI} = \frac{\frac{\mathrm{NIR}-\mathrm{RedEdge}}{\mathrm{NIR}+\mathrm{RedEdge}}}{\frac{\mathrm{NIR}-\mathrm{R}}{\mathrm{NIR}+\mathrm{R}}}$
Chlorophyll Index Red Edge	$\mathrm{CIRE} = \frac{\mathrm{NIR}}{\mathrm{RedEdge}} - 1$
Chlorophyll Vegetation Index	$\mathrm{CVI} = \mathrm{NIR}\,\frac{\mathrm{R}}{\mathrm{G}^2}$
Green Atmospherically Resistant vegetation Index	$\mathrm{GARI} = \frac{\mathrm{NIR}-(\mathrm{G}-(\mathrm{B}-\mathrm{R}))}{\mathrm{NIR}-(\mathrm{G}+(\mathrm{B}-\mathrm{R}))}$
Green Leaf Index	$\mathrm{GLI} = \frac{2\mathrm{G}-\mathrm{R}-\mathrm{B}}{2\mathrm{G}+\mathrm{R}+\mathrm{B}}$
Log Ratio	$\mathrm{logR} = \log\frac{\mathrm{NIR}}{\mathrm{R}}$
Normalized Difference Vegetation Index	$\mathrm{NDVI} = \frac{\mathrm{NIR}-\mathrm{R}}{\mathrm{NIR}+\mathrm{R}}$
Normalized Burn Ratio	$\mathrm{NBR} = \frac{\mathrm{NIR}-\mathrm{SWIR}}{\mathrm{NIR}+\mathrm{SWIR}}$
Green Blue NDVI	$\mathrm{GBNDVI} = \frac{\mathrm{NIR}-(\mathrm{G}+\mathrm{B})}{\mathrm{NIR}+\mathrm{G}+\mathrm{B}}$
Green Red NDVI	$\mathrm{GRNDVI} = \frac{\mathrm{NIR}-(\mathrm{G}+\mathrm{R})}{\mathrm{NIR}+\mathrm{G}+\mathrm{R}}$
Red Blue NDVI	$\mathrm{RBNDVI} = \frac{\mathrm{NIR}-(\mathrm{R}+\mathrm{B})}{\mathrm{NIR}+\mathrm{R}+\mathrm{B}}$
Green NDVI	$\mathrm{GNDVI} = \frac{\mathrm{NIR}-\mathrm{G}}{\mathrm{NIR}+\mathrm{G}}$
Red Edge NDVI	$\mathrm{NDVIre} = \frac{\mathrm{NIR}-\mathrm{RedEdge}}{\mathrm{NIR}+\mathrm{RedEdge}}$
Pan NDVI	$\mathrm{PNDVI} = \frac{\mathrm{NIR}-(\mathrm{R}+\mathrm{G}+\mathrm{B})}{\mathrm{NIR}+\mathrm{R}+\mathrm{G}+\mathrm{B}}$
Visible Index Green	$\mathrm{VIgreen} = \frac{\mathrm{G}-\mathrm{R}}{\mathrm{G}+\mathrm{R}}$
Norm of X (X = R, G, NIR)	$\mathrm{Norm\ X} = \frac{\mathrm{X}}{\sum \mathrm{X}}$
Blue-Wide Dynamic Range Vegetation Index	$\mathrm{BWDRVI} = \frac{0.1*\mathrm{NIR}-\mathrm{B}}{0.1*\mathrm{NIR}+\mathrm{B}}$
Chlrophyll Index Green	$\mathrm{CIgreen} = \frac{\mathrm{NIR}}{\mathrm{G}} - 1$
Green Difference Vegetation Index	$\mathrm{GDVI} = \mathrm{NIR}-\mathrm{G}$
Blue Normalized Vegetation Index	$\mathrm{BNDVI} = \frac{\mathrm{NIR}-\mathrm{B}}{\mathrm{NIR}+\mathrm{B}}$
Redness Index	$\mathrm{RI} = \frac{\mathrm{R}-\mathrm{G}}{\mathrm{R}+\mathrm{G}}$
Difference Vegetation Index or Vegetation Index Number	$\mathrm{DVI} = \frac{\mathrm{NIR}}{\mathrm{R}}$
Modified Simple Ratio	$\mathrm{MSR} = \frac{\frac{\mathrm{NIR}}{R}}{\sqrt{\frac{\mathrm{NIR}}{\mathrm{R}}+1}}$
Specific Leaf Area Vegetation Index	$\mathrm{SLAVI} = \frac{\mathrm{NIR}}{\mathrm{R}+\mathrm{SWIR}}$

R = Red; G = Green; B = Blue; NIR = Near Infrared; RedEdge = Red-Edge; SWIR = Short-wave infrared.

All the four networks are regularized by a loss mechanism that optimizes the model to learn targeted representations from the data and accurately predicts the target parameter. The latent generator with the decoder network accounts for the "*generative parameters"* and the encoder network with the regressor network accounts for the "*inference parameters"*. This is because the reconstructed data is assumed to be generated from its latent representation, which is dependent on the target parameter that makes the latent generator and the decoder network function as a "*generative model"*. The "*inference model"* consists of the probabilistic encoder that determines the latent representation from the data and a probabilistic regressor that predicts the target parameter using the latent features. The total loss $\mathcal{L}(i)$ of the proposed generative neural network can be stated, as shown in

$$\begin{aligned}\mathcal{L}(i) = & -D_{KL}\left(q\left(t|i\right) \,||\, p\left(t\right)\right) \\ & + \mathbb{E}_{q(s|i)}\left[\log\, p\left(i|s\right)\right] \\ & - \mathbb{E}_{q(t|i)}\left[D_{KL}\left(q\left(s|i\right)||\, p\left(s|t\right)\right)\right]. \end{aligned} \tag{1}$$

In the given (1), the total loss $\mathcal{L}(i)$ is a sum of three different loss terms associated with regularizing the inference and generative parameters of the proposed network. Particularly, $q(t|i)$ is a conventional feed forward regression network that produces bias (standard deviation) as an additional output

TABLE III
ANALYTICAL FEATURES FROM SENTINEL-1 SAR DATA AND THEIR EQUATIONS

Analytical SAR Features	Equations
Radar Vegetation Index	$\mathrm{RVI} = \frac{4\sigma^0_{\mathrm{VH}}}{\sigma^0_{\mathrm{VV}} + \sigma^0_{\mathrm{VH}}}$
Degree of Polarization	$\mathrm{DOP} = \sqrt{1 - \frac{4\lvert C_2\rvert}{(\mathrm{Tr}(C_2))^2}}$
Dual-pol Radar Vegetation Index	$\mathrm{DpRVI} = (1 - \mathrm{DOP}) * \frac{\lambda_1}{\lambda_1 + \lambda_2}$
Polarimetric Radar Vegetation Index	$\mathrm{PRVI} = (1 - \mathrm{DOP}) * \sigma^0_{\mathrm{VH}}$

σ^0_{VH} = Cross-polarized backscattering coefficient; σ^0_{VV} = Co-polarized backscattering coefficients; C_2 = Covariance matrix; Tr = Matrix Trace Operator; λ_1, λ_2 = Eigen values of C_2.

(therefore a probabilistic regressor). The first term represents the KL (Kullback–Leibler) divergence loss that regularizes the prediction of target with a prior. The second term represents reconstruction loss that emphasizes the reconstructed data to resemble to the input data and the third term represents the label loss that emphasizes the encoder (posterior - $q(s|i)$) to resemble to the target-specific prior $p(s|t)$.

B. Proposed Generative Network Architecture

The dynamic architecture of the generative neural network shown in Fig. 4 consists of an encoder network with an input layer of dimension "n" connected to two intermediate hidden layers of dimensions n-2 and n-4 with "tanh" activation function where "n" is the number of input features. The resultant features from the hidden layers were independently connected to two other dense layers of same dimensions (n-6, n-6) that characterize the mean and diagonal covariance of the latent space. The probabilistic regressor network shared the two hidden layers of the encoder network and consisted of a simple dense layer to produce predicted mean and standard deviation of the target parameter. A standard reparametrization trick was applied to use the mean and variance as arguments to return sampled vectors (z and r) enabling backpropagation through the network. A latent generator of dimension "n-6" was used to condition "z" on "r" by the means of KL divergence loss function. Finally, the decoder network was built with an exact inverse structure of the encoder network for the reconstruction of data from the reparametrized latent space.

IV. APPROACH FOR AGB PREDICTION

The flowchart of the AGB prediction approach is shown in Fig. 5. In the following sections each part of the flowchart is described in detail. The data preprocessing of MS and SAR data is described in Section IV-A. The process of computing analytical features from both preprocessed data and the steps for suitable data preparation as model input are stated in Section IV-B. Finally, the implementation of the developed generative model and performed experiments are described in Section IV-C.

A. Data Preprocessing

The Sentinel-2 images were acquired in Level-1C (Top of the atmosphere reflectance) format and converted to Level-2A (Bottom of the atmosphere reflectance) format including atmospheric and terrain correction using the Sen2cor processor [69]. The spectral bands at spatial resolution 10 and 20 m were used in this article and those at 20 m spatial resolution were resampled at 10 m for spatial consistency and for performing computations.

The acquired Sentinel-1 SLC product swath was split with selected bursts into a separate product. The orbit file was acquired and precise orbits are applied to the split Sentinel-1 product. The resultant product was radiometrically corrected and the calibrated SAR images were produced with pixel values that truly represent the radar backscatter of the reflecting surface. The bursts of the product were merged in the azimuth direction for a seamless image and the debursted split products of different subswaths were merged to form a single image. A subset was clipped from the single merged image of the area of interest (study area). In order to produce a polarimetric analysis ready data (ARD), we generated C2 polarimetric matrix—an incoherent polarimetric representation of second order partial polarimetric scattering matrix elements. Multilooking and speckle filtering were performed on the resultant ARD product to reduce speckle noise and generate ground range square pixels. Finally, the range Doppler terrain correction was performed to geocode and produce a final product of 10 m spatial resolution. The entire Sentinel-1 data preprocessing was performed using sentinel application platform version 8.0 software.[3]

B. Computed Features and Input Data Preparation

The preprocessed data for each season were used to compute analytical features, i.e., 25 vegetation indices from Sentinel-2 (see Table II) data and four radar vegetation indices from Sentinel-1 data (see Table III). The numerous vegetation indices consist of discrete information from the spectral and backscatter data. These vegetation indices reduce the effect of environmental conditions and compensate for atmospheric distortions. Moreover, they maximize the sensitivity to biophysical properties and minimizes topographical effects. Therefore, they can be used as input for engineering target-oriented generative features with the proposed framework.

The analytical features from Sentinel-1 data were computed using a QGIS plugin - SAR Tools [70]. In addition to the stated analytical features, ten reflectance bands of Sentinel-2 data and four polarimetric matrix elements (C_{11}, C_{12}, C_{21}, C_{22}) of the Sentinel-1 data were also considered for the input dataset. These polarimetric matrix elements are second order scattering information generated from the spatial averaging of the scattering vector $k = [S_{VV},\ S_{VH}]^T$, as stated in (2). All these computed analytical features, reflectance bands, and polarimetric matrix elements acted as a precursor for engineering abstract and target specific features using the proposed generative neural network

$$C_2 = \begin{bmatrix} C_{11} & C_{12} \\ C_{21} & C_{22} \end{bmatrix} = \begin{bmatrix} |S_{VV}|^2 & S_{VV}S^*_{VH} \\ S_{VH}S^*_{VV} & |S_{VH}|^2 \end{bmatrix}. \quad (2)$$

Reference plot sized buffers of radius 15 m were applied at each plot location to extract mean value from the computed

[3][Online]. Available: https://step.esa.int/

TABLE IV
VALIDATION STATISTICS FOR MODEL PERFORMANCE

Accuracy statistics	Equations	Validation Aspect
Mean Absolute Error	$MAE = \sum_{i=1}^{n} \lvert pre_i^{CV} - obs_i \rvert / n$	Prediction Accuracy (scale dependent)
Root-mean-squared differences	$RMSD = \sqrt{\frac{SS^{CV}}{n}}$	Prediction Precision
Coefficient of determination (cross validation)	$R^2_{CV} = 1 - SS^{CV}/SS_{tot}$	Prediction Agreement
R^2 Ratio	$R2R = R^2_{fit}/R^2_{CV}$	Overfitting

n: total number of samples; pre_i^{CV}: prediction value of sample 'i' obtained by cross validation; obs_i: observed value of sample 'i'; SS^{CV}: sum of squared differences between observed and predicted values by cross validation; SS_{tot}: sum of squared differences of each observation from overall mean; R^2_{CV}: Coefficient of determination via Cross Validation; R^2_{fit} : Coefficient of Determination via Residuals (without cross validation).

TABLE V
LIST OF SELECTED ANALYTICAL FEATURES POST A-L1 REGULARIZATION

Selected MS features	Selected SAR features	Selected DS features
1. BWDRVI_march	1. C_{11}_december	1. BWDRVI_march
2. GLI_march	2. C_{12}_december	2. GLI_march
3. normG_march	3. C_{21}_december	3. normG_march
4. VIgreen_march	4. C_{12}_june	4. CIRE3_march
5. CIRE3_march	5. C_{21}_june	5. NDVIre1_march
6. NDVIre1_march	6. PRVI_june	6. NBR2_march
7. NDVIre2_march	7. C_{12}_march	7. GLI_june
8. NDVIre3_march	8. C_{21}_march	8. normG_june
9. NBR1_march	9. PRVI_march	9. VIgreen_june
10. NBR2_march	10. C_{12}_september	10. CCCI1_june
11. GLI_june	11. C_{21}_september	11. NBR2_june
12. normG_june		12. VIgreen_september
13. VIgreen_june		13. RI_september
14. CCCI1_june		14. CCCI1_septemeber
15. CCCI2_june		15. NDVIre1_september
16. NBR2_june		16. NBR2_september
17. GLI_september		17. CIRE3_december
18. normG_september		18. C_{11}_december
19. VIgreen_september		19. C_{12}_december
20. RI_september		20. C_{21}_december
21. CCCI1_september		21. PRVI_december
22. NDVIre1_september		22. C_{12}_june
23. NBR2_september		23. C_{21}_june
24. normR_december		24. PRVI_june
25. VIgreen_december		25. C_{11}_march
26. CIRE3_december		26. C_{12}_march
		27. C_{21}_march
		28. C_{22}_march
		29. PRVI_march
		30. C_{12}_september
		31. C_{21}_september
		32. DOP_september
		33. PRVI_september

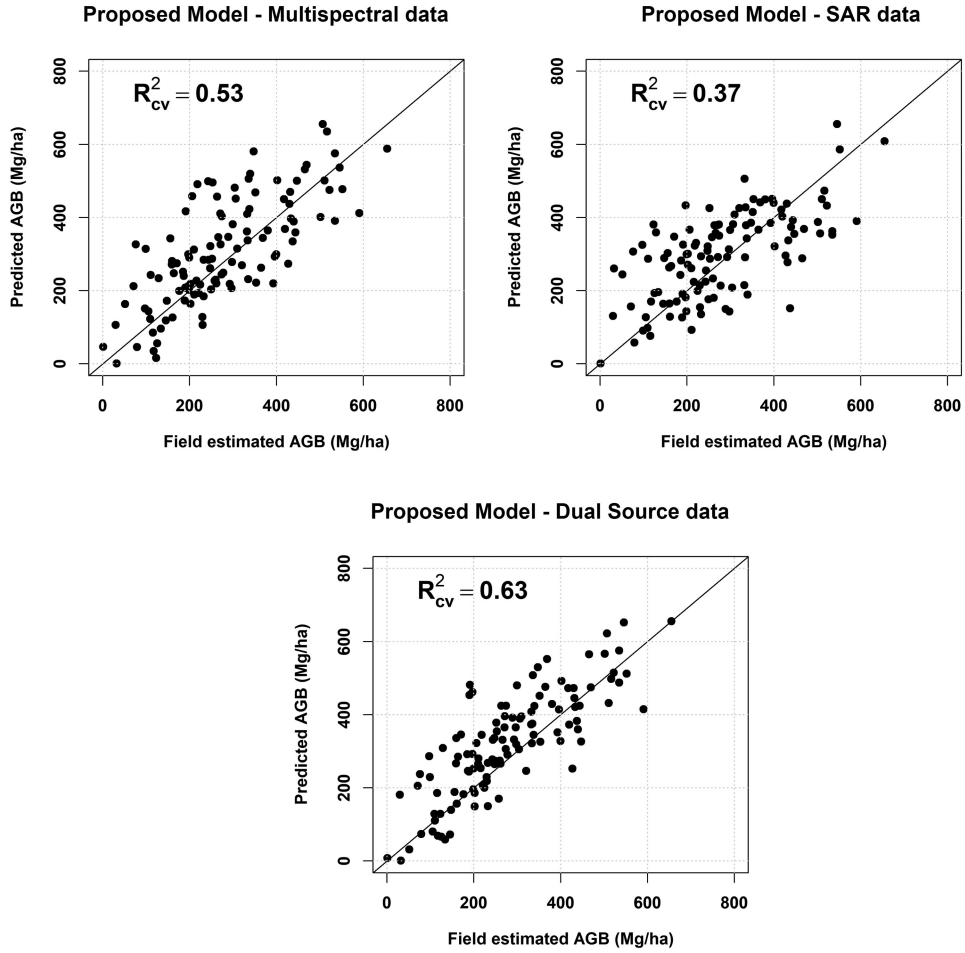

Fig. 6. Regression scatterplots of the proposed model for single source and DS data.

TABLE VI
PERFORMANCE METRICS OF MODELS DEVELOPED USING MS, SAR, AND DS DATA

	MS				SAR				DS			
Models	**R^2_{cv}**	**RMSD%**	**R2R**	**MAE**	**R^2_{cv}**	**RMSD%**	**R2R**	**MAE**	**R^2_{cv}**	**RMSD%**	**R2R**	**MAE**
Proposed	0.53	37.8	1.3	83.1	0.37	38.9	1.4	87.1	0.63	34.6	1.3	73.6
MLP	0.15	72.9	1.9	162.5	0.08	75.4	1.8	172.7	0.21	74.6	1.9	165.7
GLM	0.44	46.7	1.4	80.9	0.19	51.7	1.8	117.6	0.45	36.9	1.5	82.7
XGBoost	0.34	39.6	2.5	88.2	0.18	53.1	4.3	117.3	0.36	39.6	2.6	91.9
RF	0.44	39.7	1.8	85.3	0.1	47.66	12.4	107.9	0.45	37.16	1.8	83.5

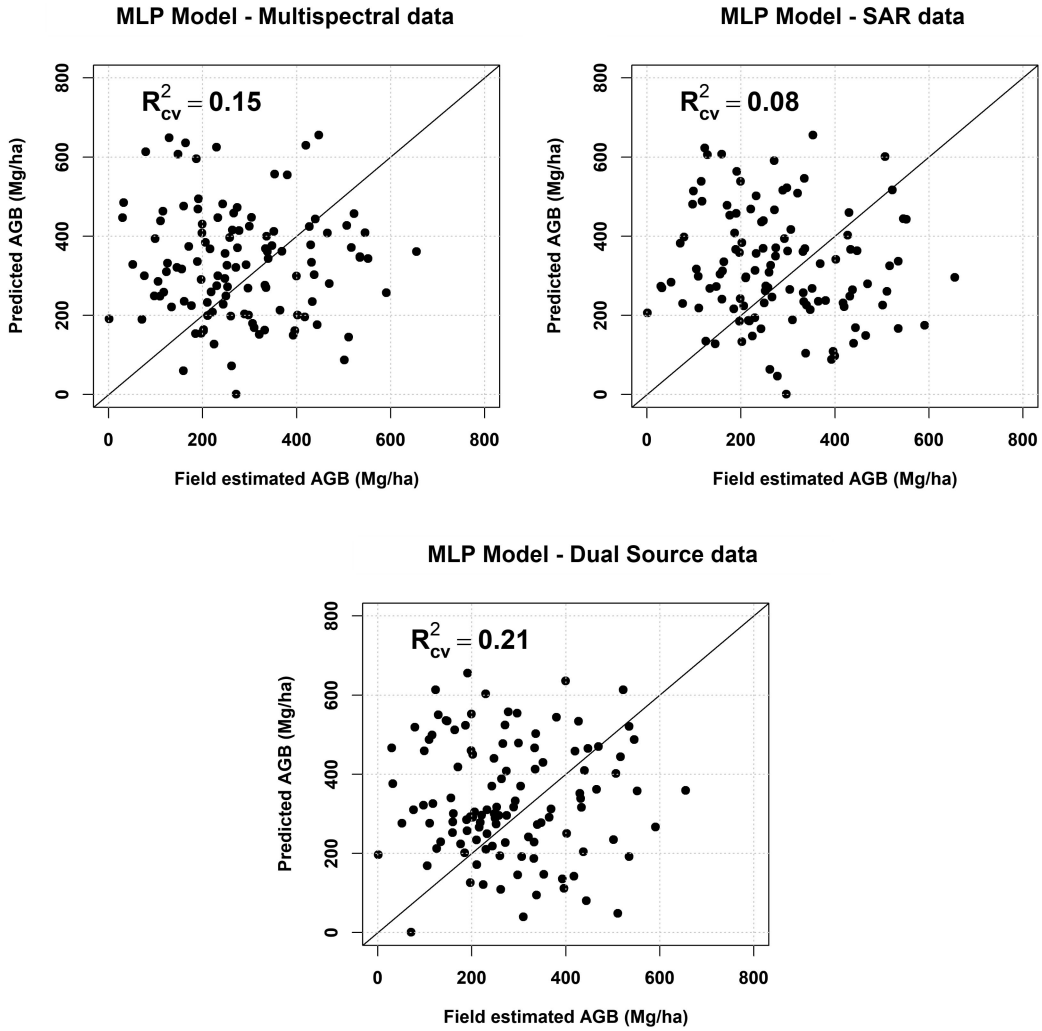

Fig. 7. Regression scatterplots of MLP model for single source and DS data.

vegetation indices and a plot level training dataset is prepared. The missing values (if any) in the dataset were replaced using the median operator and the range of observations in each dataset were standardized using a standard scaler that subtracts the mean and scales to unit variance. The prepared dataset was exported to standard binary file format that stores the shape and information necessary for performing operations with the proposed generative neural network model. In order to reduce the model complexity, adaptive L1 (A-L1) regularization was applied to the prepared dataset to limit the number of input variables. The entire process was carried out to prepare three separate sets of data based on the data source, i.e., MS dataset, SAR dataset, and DS dataset. Finally, a clean, standardized and regularized input dataset was fed to the developed generative neural network.

C. Model Implementation and Experiments

The developed architecture of the proposed generative neural network is dynamic and depends on the number of analytical features selected post A-L1 regularization. Therefore, the number of network filters for each layer change for each of the three datasets based on the schema of the dynamic architecture shown in Fig. 4. The developed generative neural network was trained with a batch size of 10 and a total of 500 epochs. The dense layers of the network were L2 regularized to keep the weights and biases small and reduce the likelihood of overfitting. The network was trained by using a K-fold stratified cross-validation method with five folds. The model was implemented using open-source software library "TensorFlow" on a Python API. The training of the network was performed on a 134 GB RAM NVIDIA GeForce RTX 3090 GPU on a Linux based OS. A pseudocode of the proposed model can be accessed from GitHub repository using the link.[4]

The experiments were designed to quantify the improvement in AGB predictions and the refinement in the quality of feature space achieved using the proposed model. We used multiple models based on different techniques such as linear, bagging, boosting, and neural networks to compare the results with the proposed model. In particular, we used generalized linear

[4][Online]. Available: https://github.com/parth-unitn/RSGenFeatures.git

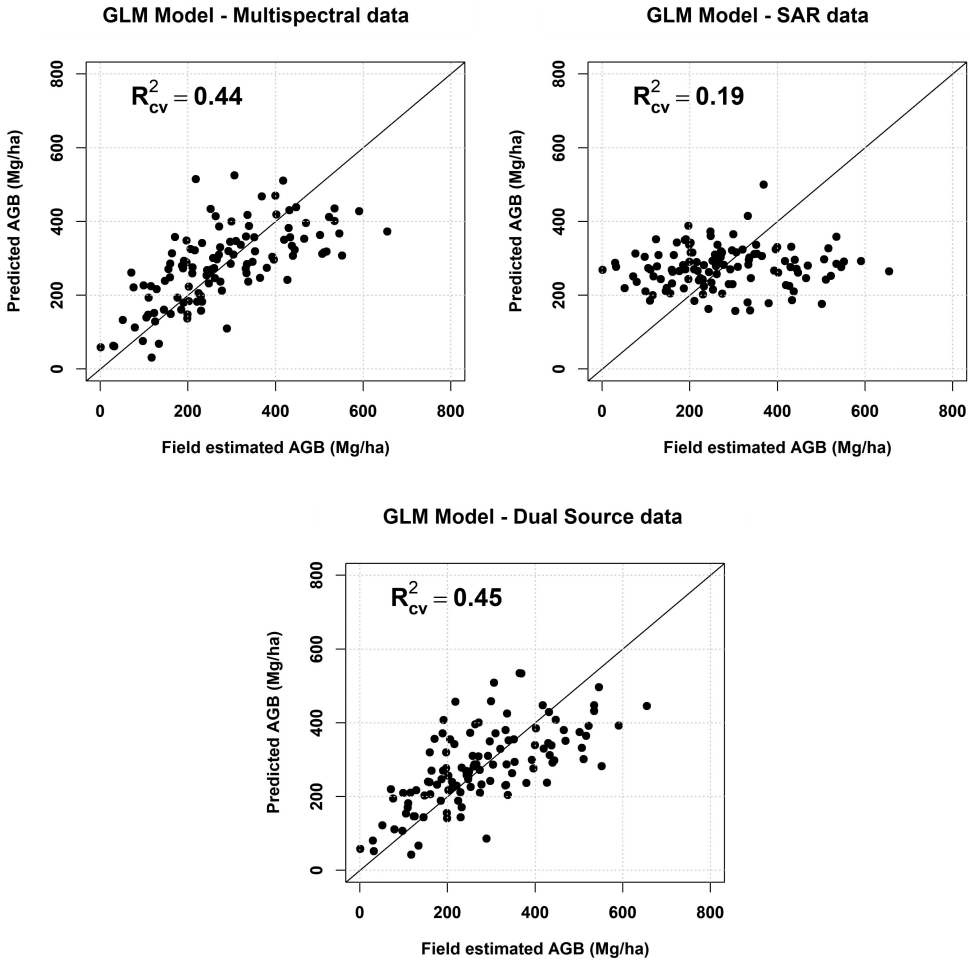

Fig. 8. Regression scatterplots of GLM model for single source and DS data.

model (GLM), RF, extreme gradient boosting (XGBoost), and a multilayer perceptron model (MLP) for comparing model performance. The structure of the MLP model was same as structure of the regressor unit used with the proposed model to quantify the improvement delivered by the generative process in model performance (i.e., improvement achieved by the probabilistic regressor network as compared to a nonprobabilistic regressor network with same structure). All the comparative models were fine-tuned for optimal performance according to respective requirements using random hyperparameter search (for RF), early stopping (for XGBoost, MLP), and adaptive moment optimization (for MLP). All the comparative models were 5-fold cross validated and trained using A-L1 regularized features.

Model prediction agreement were evaluated using cross validated R-squared score ($R^2{}_{cv}$), prediction precision was estimated using the root mean squared percentage difference (RMSD), model overfitting was quantified using the R-squared ratio (R2R) and scale-depended prediction accuracy was measured using the mean absolute error (MAE). The equations of these statistical performance metrics and the respective validation aspect are given in Table IV. In order to compare the quality of the feature space, we used the t-SNE (t-distributed stochastic neighbor embedding) technique and visualized the A-L1 regularized analytical features (input for GLM, RF, XGBoost, MLP) and the generative features from latent space (input for the probabilistic regressor of the proposed model) on a 2-D plane color-coded with field estimated AGB. The t-SNE visualization were used to analyze the orientation of the latent space with respect to the field estimated AGB. These analytical and generative features were scored using feature importance derived from an independent gradient boosting machine (GBM) algorithm for quantitative assessment of their feature contribution. The GBM-based feature importance scores were computed using a standard permutation feature importance algorithm. Finally, we also generated an AGB map of the Trentino region using the best proposed model and performed correlation analysis using 55 additional reference AGB plots for independent site validation.

V. Results

A. Analytical Features Selected Post A-L1 Regularization

The list of the selected analytical features post A-L1 regularization is given in Table V. The regularized datasets consisted of 26 features for MS, 11 features for SAR, and 33 features for

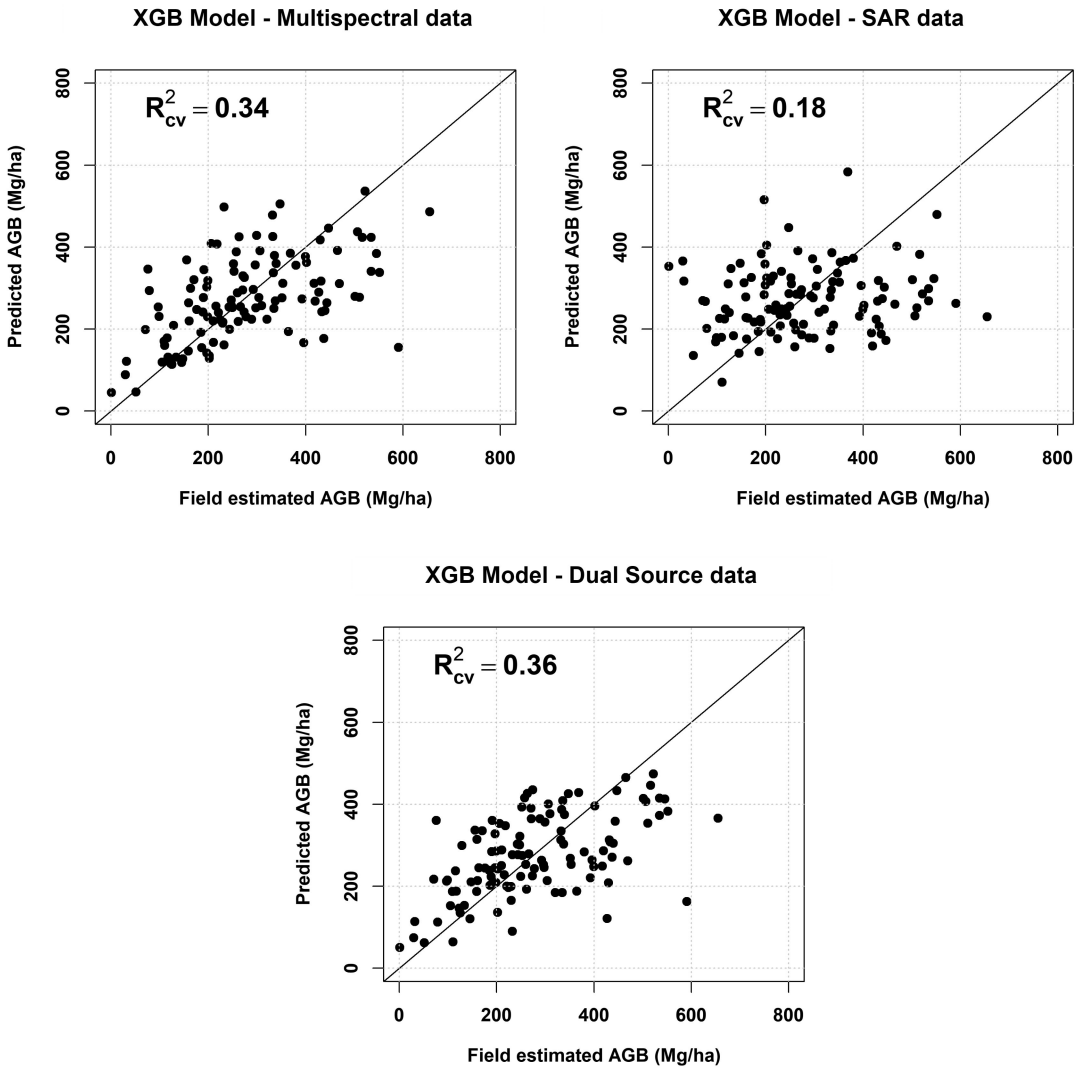

Fig. 9. Regression scatterplots of XGB model for single source and DS data.

the DS dataset. The 26 features of the regularized MS dataset consisted of ten features from the spring season, six features from the summer season, 7 features from the autumn season, and three features from the winter season. Thus, the regularization showed different degree of relevance for different seasons for the MS dataset. A major contribution of the red-edge spectrum (nine features) and short wave infrared spectrum (four features) was observed in the regularized MS dataset. The 11 features of the regularized SAR dataset mainly consisted of polarimetric matrix elements (C_{12}, C_{21}) from all seasons, C_{11} from the winter season and PRVI from summer and autumn season. The 33 features of the regularized DS dataset consist of 17 MS features and 16 SAR features.

B. Predictive Analysis and AGB Mapping

The regression scatterplots for the Proposed, MLP, GLM, XGBoost, and RF model representing field estimated AGB versus the predicted AGB are shown in Figs. 6–10, respectively. The five-fold cross-validated model performance metrics for model agreement ($R^2{}_{cv}$), prediction precision (RMSD%), overfitting (R2R), and prediction bias (MAE) for all developed models and different datasets are given in Table VI.

The proposed model delivered best results with respect to all considered performance metrics for all the three datasets. Particularly, the proposed model obtained the best performance on DS data with an agreement score $R^2{}_{cv} = 0.63$ and least overfitting score R2R $= 1.3$. The model also delivered the best prediction precision RMSD% $= 34.6$ and least prediction bias MAE $= 73.6$ Mg/ha. The proposed model achieved better prediction precision (RMSD% $= 34.6 - 38.9$) and less overfitting (R2R $= 1.3 - 1.4$) as compared to MLP (RMSD% $= 72.9$–75.4 and R2R $= 1.8$–1.9) in spite of an identical neural structure of the regressor unit of the proposed model and the MLP. Also, the analytical features had a higher dimensionality (n) compared to the generative features (n-6) but the latter improved model performance metrics for all the three datasets.

With respect to the datasets considered, all examined models performed least accurately on SAR data (RMSD $= 38.9$–75.4 and MAE $= 87.1$–172.7). This result was anticipated as C-band data are characterized by low canopy penetration. However, the proposed model assisted in improving the model predictions

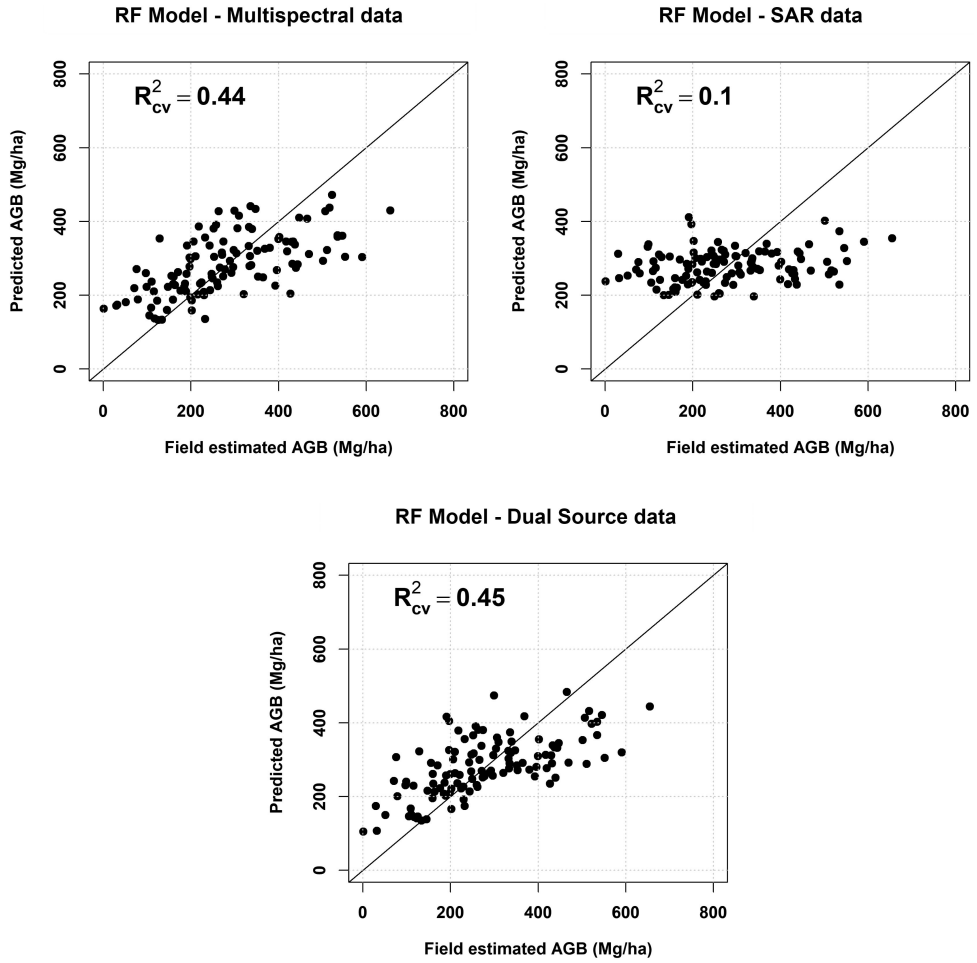

Fig. 10. Regression scatterplots of RF model for single source and DS data.

with SAR data (RMSD = 38.9 and MAE = 87.1). The prediction bias was reduced by the proposed model (MAE = 87.1) as compared to the conventional models despite the intrinsic wavelength dependent limitations of the SAR data. All models performed better with MS data as compared to SAR data but the combined DS data delivered highest model performances in terms of precision ($R^2_{cv} = 0.63$, RMSD% = 34.6, R2R = 1.3, and MAE = 73.6). Thus, the proposed model demonstrated a successful and more effective approach for seamless data fusion for modeling AGB.

Among the considered tree based models (RF and XGBoost), the RF model achieved better overall agreement ($R^2_{cv} = 0.45$) than XGBoost ($R^2_{cv} = 0.36$). Also, XGBoost produced higher overall prediction bias (MAE = 91.9) than RF (MAE = 83.5) for all datasets. Overall, RF model performed better than XGBoost in the tree based model category. Finally, in the neural network category, the MLP model delivered inaccurate predictions and showed higher overfitting compared to the GLM and the proposed model. The MLP model produced the least agreement for SAR data ($R^2_{cv} = 0.08$) with overall high prediction errors (MAE >160). Although, the proposed model provided an improved model performance as compared to the conventional neural network model (MLP) w.r.t all assessment metrics. Overall, the proposed generative neural network performed better than considered conventional models such as GLM and tree-based algorithms.

Fig. 12 shows the AGB map obtained by the proposed model on the analyzed area. A strong correlation can be observed among prediction of the proposed model and 55 additional reference data plots (locations shown in Fig. 12). Fig. 13 shows the correlation scatter plot and the computed Pearson correlation coefficient (R). The Pearson correlation coefficient for the 55 reference plots and the mapped AGB values was R = 0.66. Thus, a high correlation achieved for these independent reference plots (not used for training – testing experiments) indicated a robustness of the proposed model on new data or potentially on different sites.

C. Two-Dimensional t-SNE Visualization of Feature Spaces (Analytical and Generative) and Feature Importance

The t-SNE scatterplots of generative features and analytical features for MS, SAR, and DS datasets are shown in Fig. 11. The t-SNE scatterplots for all three datasets indicated that the latent space of the proposed model depicting generative features is highly ordered as compared to the input feature space depicting analytical features. The 2-D t-SNE visualization of a higher dimensional latent space indicated that the arrangement of the

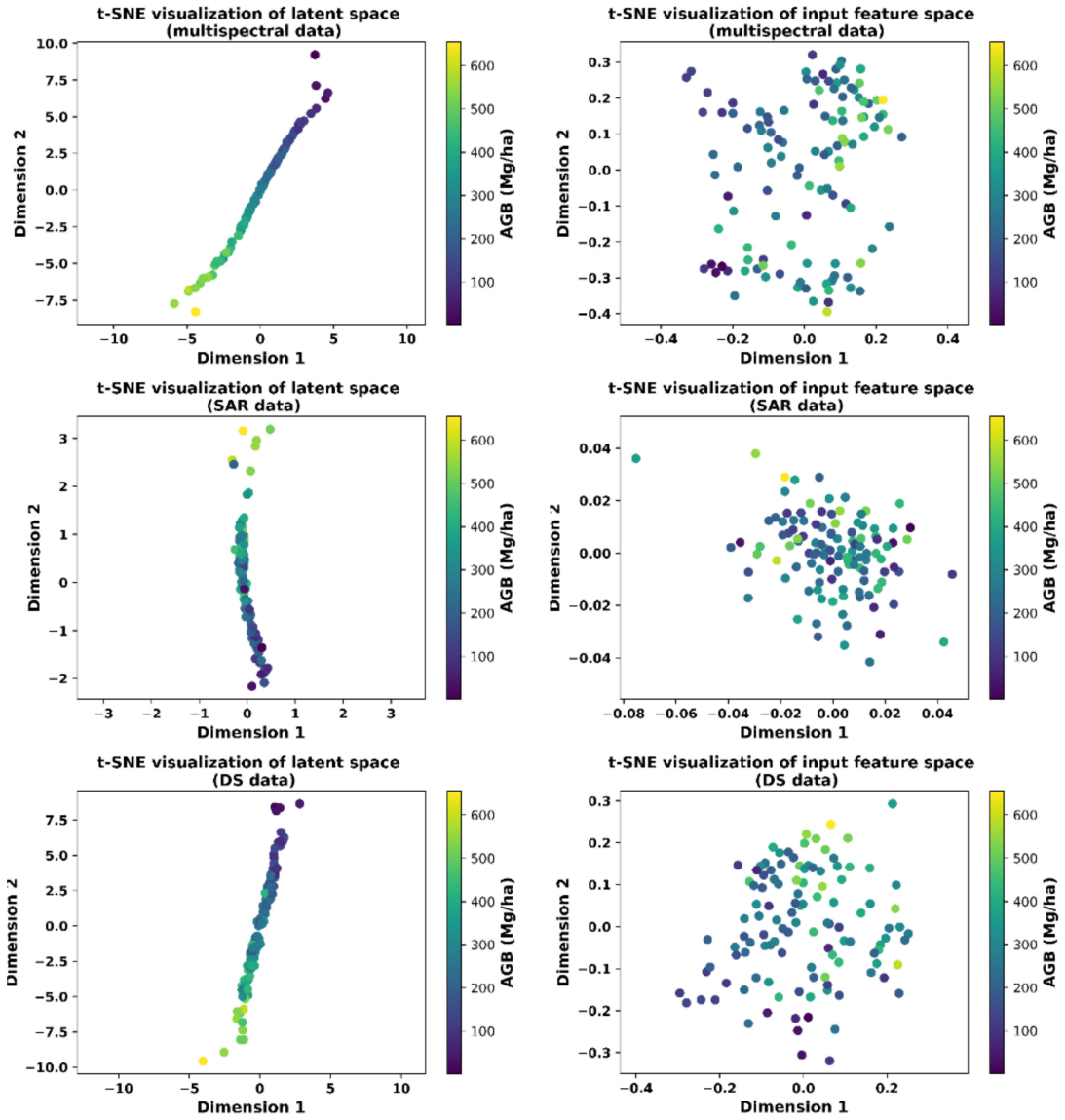

Fig. 11. t-SNE scatterplots of latent space and input feature space for MS, SAR, and DS data.

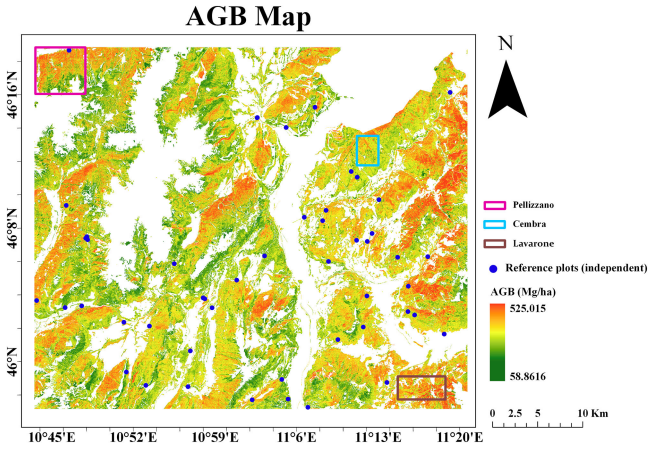

Fig. 12. AGB Map of autonomous province of Trento using best proposed model.

generative features was directional and oriented towards the target AGB. However, the 2-D t-SNE visualization of input feature space was nondirectional and showed no specific orientation towards AGB. The directional orientation of generative features w.r.t target AGB values improved the generalization of the proposed model by decreasing model overfitting and prediction bias simultaneously (R2R = 1.3 – 1.4 and MAE = 73.6 – 83.1).

The t-SNE scatterplots of the input feature space for all datasets (see Fig. 11 – Left) show an unordered distribution and produced no AGB associated variations. Although, the t-SNE scatterplots of latent space for all datasets (see Fig. 11 – Right) have one dimension clearly associated with variability of target AGB. Also, a greater degree of target association was observed for MS and DS latent space as compared to SAR latent space. A few observations from the SAR latent space from the range of 0 to100 Mg/ha were at the point (x, y) = (00) that had

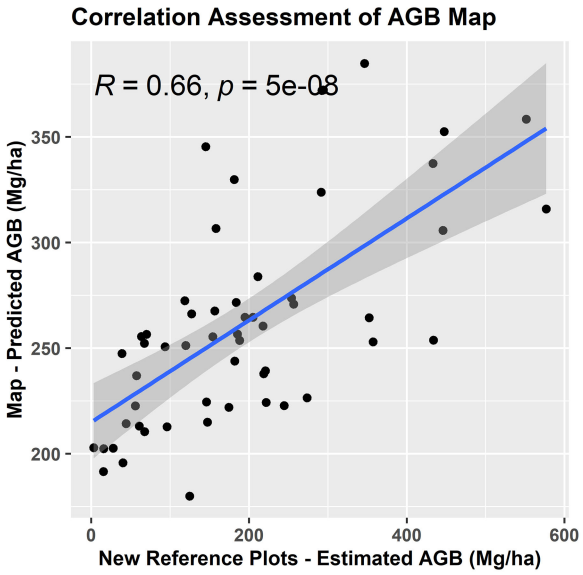

Fig. 13. Correlation assessment of the AGB map.

TABLE VII
COEFFICIENTS OF THE ALLOMETRIC EQUATIONS OF [74] AND WD FROM (IPCC 2003) [75]. THE WD IS EXPRESSED IN KG/M^3

	WD	α	γ	δ	d_0
Abies alba	400	0.000163	1.70656	0.941905	3.69465
Broadleaves	580	0.000055	1.942089	1.00642	4.0091
Larix decidua	460	0.000108	1.407756	1.341377	3.69465
Picea abies	400	0.000177	1.564254	1.051565	3.69465
Pinus cembra	420	0.000188	1.613713	0.985266	3.69465
Pinus nigra	420	0.000129	1.763086	0.938445	3.69465
Pinus sylvestris	420	0.000102	1.918184	0.830164	3.69465

higher frequency of observations from mid-range AGB (300 to 400 Mg/ha). These disassociated observations explained the inferior results for SAR data as compared to the other data using the proposed model.

The plots of scaled feature importance versus the ten most important analytical and generative features are shown in Fig. 14. The slope of the feature importance trend line for analytical features is greater than that for generative features. The relative feature importance of analytical features scaled down at higher rate as compared to generative features. This is because only a few among all the analytical features significantly contributed to the accurate prediction of AGB. However, in case of generative features, a greater number of features provided significant contribution (see Fig. 14) for an accurate AGB prediction as compared to the analytical features. This indicated that the overall feature importance of generative features was higher as compared to that of analytical features. This also explains the role of generative features in delivering better prediction results from the performed experiments.

VI. DISCUSSION

In this article, we proposed a generative neural network with a dynamic architecture that has been used on satellite MS and SAR

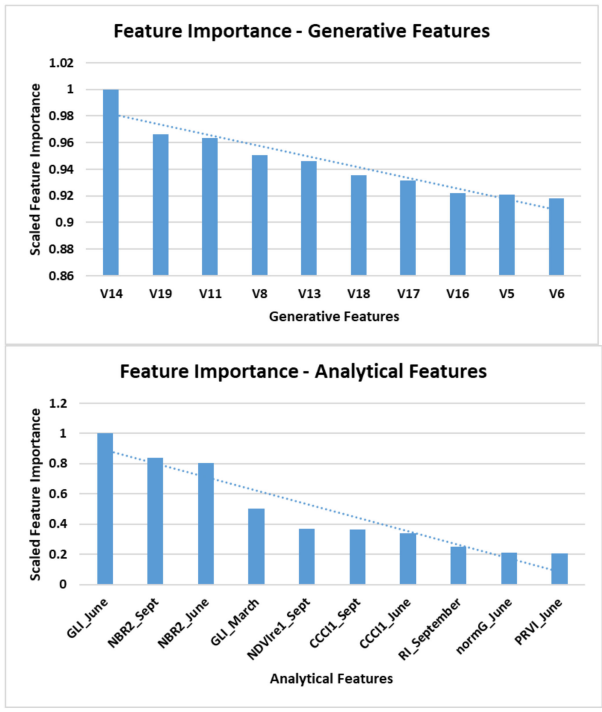

Fig. 14. Feature Importance graph for generative and analytical features.

remote sensing data for modeling plot level forest AGB. The key elements of modeling consisted of operationalizing the triple loss mechanism, producing target oriented generative features, and using a probabilistic regressor to perform predictions. This framework was proposed for dealing with the various issues identified in the literature related to the use of satellite remote sensing data for forest AGB mapping. The results achieved from the performed experiments have been analyzed with respect to the contemporary literature in this section.

Studies that used satellite remote sensing data for AGB prediction highlighted a common drawback in terms of data saturation and low prediction precision [18], [26], [71]. Our article analyzed multiple models for different datasets and found two effective ways to reduce the bias and data saturation. The first proposed way is fusion of multisensor data as this increases the number of features (and, hence, the information) that can reduce saturation for predicting higher AGB values. The second proposed way is by extracting targeted features. In case the multisensor data are not available, engineering features to induce targeted properties in the feature space can also reduce the saturation and increase prediction precision with satellite remote sensing data. In this article, we quantitatively proved that the two stated ways are effective for increasing prediction precision and reducing saturation. The metric RMSD% was significantly better for the proposed approach indicating the increased prediction precision. Moreover, a better concurrence achieved by the proposed model for a higher range of AGB values indicated reduced model saturation. This was quantitatively reflected by a higher r-squared score and can be graphically observed with regression scatterplots that show greater agreement for higher AGB values.

The analysis performed in [18] suggested calibration of the model within the range of AGB values to minimize the risk of induced prediction bias and recommended a need for AGB-oriented sensors. Forest are diverse in terms of species, density, type and distribution. Thus, designing AGB-oriented sensors for satellites would be complex and not an economically viable solution. However, designing methods to effectively engineer data and features to orient them for AGB prediction is a viable solution. This aspect was presented in the form of a probabilistic regressor network that tracks the label loss and coordinates with the latent generator to produce AGB-oriented features reducing the need for AGB-oriented sensors. In addition to regularization and dimensionality reduction of the data, our article showcased a disentanglement procedure that orients one dimension of the features to display target specific variance and thereby improving the performance of the model. Moreover, the fusion of optical and SAR data for modeling forest AGB is also a challenging task. The proposed model provided a mechanism for high-level feature fusion that generated homogenous and compressed fusion features at the latent space.

The regression algorithm used for modeling predominantly affects the prediction accuracy of the model. Multiple comparative studies that used different machine learning regression algorithms for the prediction of forest AGB from satellite RS data produced diverse results [26], [66], [72]. The comparison of these studies in literature for determining the best suitable regression algorithm is difficult due to different initial conditions (data, samples, features). The number of samples used and the type of features selected can also affect the performance of a model. Thus, the same model can perform differently by changing the initial conditions. Accordingly, the identification of the baseline model remains an issue for AGB modeling. In simple terms, it is difficult to have one baseline model that can perform best for all initial conditions. Also, the study in [66] compared a few standard machine learning algorithms and a stacked sparse autoencoder (feed forward neural network) to prove the superiority of the latter. However, the article had used random splitting of dataset (3:1) and our article that used stratified cross-validation found that feed forward neural networks are highly prone to overfitting. This problem was resolved by the idea of a robust and integrated probabilistic regressor that encourages the posterior to resemble to the AGB specific prior that can reduce the prediction bias induced by the initial conditions. This can be specifically observed from Fig. 13, where the model was applied to additional field plot samples that were not used during training of the model. The correlation plot showed that prediction bias slightly increases for extreme values of AGB but the model overall retained a strong correlation between the predicted and field estimated AGB. This shows that the proposed approach can be effectively replicated on new data or potentially new sites.

Another important aspect of this article has been to automate the process of balancing the bias-variance tradeoff of the prediction algorithm. In this article [73], eight-machine learning models were evaluated for the prediction of forest AGB using satellite remote sensing data. The article outlined the problem of stabilizing the prediction bias with change in the forest types, sampling methods, and dependence of feature importance on the deployed model. The article used 13 features for modeling and observed a high variance in the importance of the same feature for different models. The article also highlighted that the process of hyperparameter optimization for each model and selection of the best model was time consuming. Also, the entire process was automated for achieving optimal results with a less complex and time efficient computations.

Overall, our article effectively deals with various problems identified in the literature by providing a robust solution in form of a generative modeling architecture. However, a prime limitation of the proposed model is that it uses a neural network based regressor unit and cannot be replaced by any other contemporary regression algorithm (e.g., Random Forest or XGBoost). The generative architecture requires a neural network unit to update weights and produce targeted generative features. Thus, it reduces the scope of testing other regression algorithms with the proposed architecture. Moreover, the architecture of the proposed model is complex with separate inference and generative parameters. Therefore, it is difficult to use a neural architecture search algorithm to optimize the number of filters and layers of the model. This limits the strategy of determining the most optimal architecture of the proposed model.

VII. Conclusion

This article has proposed a generative approach for modeling forest AGB using satellite RS data. The results demonstrated the superiority of generative features over conventional analytical features extracted from satellite RS data for AGB prediction. The proposed dynamic architecture and the triple loss mechanism generate target specific features that showed improvement for all prediction metrics (agreement, precision, and overfitting) in our experiments. Moreover, the proposed model also demonstrated its effectiveness in efficient feature fusion and compression. It was conclusive from experiments that it is difficult to completely eliminate the factor of data saturation but the proposed model substantially reduced it thereby increasing the reliability of satellite RS data for AGB prediction. The future work of this article may aim at testing the proposed framework to predict other forest biophysical variables and parameters from a different RS application. Moreover, the aspect of model saturation can be studied in more detail for all such biophysical variables including AGB using the proposed features. The proposed framework could also be modified and used for classification tasks such as tree species or land-use land-cover classification.

Appendix A

The allometric equations used for the estimation of the AGB of each tree are based on the equations published in [74] multiplied by the wood density (WD) of each species (IPCC 2003) [75]. The resulting equation for the estimation of tree AGB in kilograms is given by

$$\mathrm{AGB} \;=\; \mathrm{WD} * \alpha * (\mathrm{DBH} - d_0)^{\gamma} * H^{\delta} \qquad \text{(A1)}$$

where DBH is the diameter in centimetres and H the height in meters. The coefficients used for the different species are given in Table VII.

REFERENCES

[1] U. B. Gewali, S. T. Monteiro, and E. Saber, "Gaussian processes for vegetation parameter estimation from hyperspectral data with limited ground truth," *Remote Sens.*, vol. 11, no. 13, Jul. 2019, Art. no. 1614, doi: 10.3390/rs1113161.

[2] B. Petrovska, E. Zdravevski, P. Lameski, R. Corizzo, I. Štajduhar, and J. Lerga, "Deep learning for feature extraction in remote sensing: A case-study of aerial scene classification," *Sensors*, vol. 20, no. 14, 2020, Art. no. 3906, doi: 10.3390/s20143906.

[3] J. Heaton, "An empirical analysis of feature engineering for predictive modeling," in *Proc. SoutheastCon*, IEEE, Piscataway, NJ, USA, 2016, pp. 1–6, doi: 10.1109/secon.2016.7506650.

[4] P. Naik and A. Kumar, "A stochastic approach for automatic collection of precise training data for a soft machine learning algorithm using remote sensing images," in *Advances in Intelligent Systems and Computing*. Berlin, Germany: Springer, 2021, pp. 285–297, doi: 10.1007/978-981-16-2712-5_24.

[5] P. Sivaraj, A. Kumar, S. R. Koti, and P. Naik, "Effects of training parameter concept and sample size in possibilistic c-Means classifier for pigeon pea specific crop mapping," *Geomatics*, vol. 2, no. 1, pp. 107–124, Feb. 2022, doi: 10.3390/geomatics2010007.

[6] C. Poultney *et al.*, "Efficient learning of sparse representations with an energy-based model," in *Proc. Conf. Adv. Neural Inf. Process. Syst.*, 2006, pp. 1137–1144.

[7] D. E. Rumelhart and G. E. Hintont, "Learning representations by back-propagating errors," *Nature*, vol. 323, no. 6088, pp. 533–536, Oct. 1986, doi: 10.1038/323533a0.

[8] M. Monteleone, "NooJ local grammars and formal semantics: Past participles vs. adjectives in Italian," *Commun. Comput. Inf. Sci.*, vol. 607, no. 8, pp. 83–95, 2016.

[9] S. Mohanty and G. Singh, "Fully polarimetric synthetic aperture radar indices for scintillation observation," in *Proc. URSI Asia-Pacific Radio Sci. Conf.*, 2019, pp. 1–4.

[10] N. G. Silleos, T. K. Alexandridis, I. Z. Gitas, and K. Perakis, "Vegetation indices: Advances made in biomass estimation and vegetation monitoring in the last 30 years," *Geocarto Int.*, vol. 21, no. 4, pp. 21–28, 2006.

[11] L. C. G. David, R. A. Pula, C. N. Cabaccan, B. J. J. Esguerra, and A. H. Ballado, "Assessment of LiDAR-derived height metrics for mapping mangrove forest using object-based method," in *Proc. 37th Asian Conf. Remote Sens.*, 2016, pp. 796–805.

[12] J. Xue and B. Su, "Significant remote sensing vegetation indices: A review of developments and applications," *J. Sensors*, vol. 2017, pp. 1–17, 2017, doi: 10.1155/2017/1353691.

[13] G. De Luca, J. M. N. Silva, S. Di Fazio, and G. Modica, "Integrated use of sentinel-1 and sentinel-2 data and open-source machine learning algorithms for land cover mapping in a Mediterranean region," *Eur. J. Remote Sens.*, vol. 55, no. 1, pp. 52–70, 2022.

[14] E. Halme, P. Pellikka, and M. Mõttus, "Utility of hyperspectral compared to multispectral remote sensing data in estimating forest biomass and structure variables in finnish boreal forest," *Int. J. Appl. Earth Observ. Geoinf.*, vol. 83, 2019, Art. no. 101942.

[15] R. D. Sheridan, S. C. Popescu, D. Gatziolis, C. L. S. Morgan, and N. W. Ku, "Modeling forest aboveground biomass and volume using airborne LiDAR metrics and forest inventory and analysis data in the Pacific Northwest," *Remote Sens.*, vol. 7, no. 1, pp. 229–255, 2015.

[16] L. A. Ruiz, T. Hermosilla, F. Mauro, and M. Godino, "Analysis of the influence of plot size and LiDAR density on forest structure attribute estimates," *Forests*, vol. 5, no. 5, pp. 936–951, 2014.

[17] Z. Wu, D. Dye, J. Stoker, J. Vogel, M. Velasco, and B. Middleton, "Evaluating LiDAR point densities for effective estimation of aboveground biomass," *Int. J. Adv. Remote Sens. GIS*, vol. 5, no. 1, pp. 1483–1499, 2016.

[18] N. Jha *et al.*, "The real potential of current passive satellite data to map aboveground biomass in tropical forests," *Remote Sens. Ecol. Conservation*, vol. 7, no. 3, pp. 504–520, 2021.

[19] P. Naik, M. Dalponte, and L. Bruzzone, "Prediction of forest aboveground biomass using multitemporal multispectral remote sensing data," *Remote Sens.*, vol. 13, no. 7, Mar. 2021, Art. no. 1282, doi: 10.3390/rs13071282.

[20] T. T. C. Tuong, H. Tani, X. Wang, N. Q. Thang, and H. M. Bui, "Combination of SAR polarimetric parameters for estimating tropical forest aboveground biomass," *Polish J. Environ. Stud.*, vol. 29, no. 5, pp. 3353–3365, 2020.

[21] P. Naik, M. Dalponte, and L. Bruzzone, "A comparison on the use of different satellite multispectral data for the prediction of aboveground biomass," in *Proc. Image Signal Process. Remote Sens. XXVI*, Bellingham, WA, USA, 2020, Art. no. 1153315, doi: 10.1117/12.2572807.

[22] T. D. Pham, N. Yokoya, D. T. Bui, K. Yoshino, and D. A. Friess, "Remote sensing approaches for monitoring mangrove species, structure, and biomass: Opportunities and challenges," *Remote Sens.*, vol. 11, no. 3, p. 230, 2019.

[23] Y. Zhang, S. Liang, and L. Yang, "A review of regional and global gridded forest," *Remote Sens.*, vol. 11, no. 23, 2019, Art. no. 2744.

[24] S. Abbas, M. S. Wong, J. Wu, N. Shahzad, and S. M. Irteza, "Approaches of satellite remote sensing for the assessment of above-ground biomass across tropical forests: Pan-tropical to national scales," *Remote Sens.*, vol. 12, no. 20, 2020, Art. no. 3351.

[25] S. Sinha, C. Jeganathan, L. K. Sharma, and M. S. Nathawat, "A review of radar remote sensing for biomass estimation," *Int. J. Environ. Sci. Technol.*, vol. 12, no. 5, pp. 1779–1792, 2015.

[26] Y. Li, M. Li, C. Li, and Z. Liu, "Forest aboveground biomass estimation using Landsat 8 and Sentinel-1A data with machine learning algorithms," *Sci. Rep.*, vol. 10, no. 1, pp. 1–12, 2020.

[27] P. Naik, M. Dalponte, and L. Bruzzone, "A disentangled variational autoencoder for prediction of above ground biomass from hyperspectral data," in *Proc. IEEE Int. Geosci. Remote Sens. Symp.*, Piscataway, NJ, USA, 2021, pp. 2991–2994, doi: 10.1109/igarss47720.2021.9554415.

[28] G. Sandberg, L. M. H. Ulander, J. E. S. Fransson, J. Holmgren, and T. Le Toan, "L- and P-band backscatter intensity for biomass retrieval in hemiboreal forest," *Remote Sens. Environ.*, vol. 115, no. 11, pp. 2874–2886, 2011.

[29] M. A. Tanase, R. Panciera, K. Lowell, J. Hacker, and J. P. Walker, "Estimation of forest biomass from L-band polarimetric decomposition components cooperative research centre for spatial information, the University of Melbourne Airborne Research Australia, school of the environment, Flinders University department of Ci," in *Proc. IEEE Int. Geosci. Remote Sens. Symp.*, Jul. 2013, pp. 949–952, doi: 10.1109/igarss.2013.6721318.

[30] S.- Umeå, L. M. H. Ulander, E. Blomberg, and M. J. Soja, "Measurements of forest biomass change using L-and P-band SAR backscatter," in *Proc. IEEE Int. Geosci. Remote Sens. Symp.*, 2017, pp. 5818–5821.

[31] M. Schlund and M. W. J. Davidson, "Aboveground forest biomass estimation combining L- and P-band SAR acquisitions," *Remote Sens.*, vol. 10, no. 7, 2018, Art. no. 1151.

[32] M. L. R. Sarker, J. Nichol, H. B. Iz, B. B. Ahmad, and A. A. Rahman, "Forest biomass estimation using texture measurements of high-resolution dual-polarization C-band SAR data," *IEEE Trans. Geosci. Remote Sens.*, vol. 51, no. 6, pp. 3371–3384, Jun. 2013.

[33] R. J. L. Argamosa *et al.*, "Modelling above ground biomass of mangrove forest using sentinel-1 imagery," *ISPRS Ann. Photogrammetry Remote Sens. Spatial Inf. Sci.*, vol. 4, no. 3, pp. 13–20, 2018.

[34] N. N. Askar, W. Phairuang, P. Wicaksono, and T. Sayektiningsih, "Estimating aboveground biomass on private forest using sentinel-2 imagery," *J. Sensors*, pp. 1–11, 2018, doi: 10.1155/2018/6745629.

[35] A. B. Baloloy *et al.*, "Estimation of mangrove forest aboveground biomass using multispectral bands, vegetation indices and biophysical variables derived from optical satellite imageries: Rapideye, planetscope and Sentinel-2," *ISPRS Ann. Photogrammetry Remote Sens. Spatial Inf. Sci.*, vol. 4, no. 3, pp. 29–36, 2018.

[36] M. E. J. Cutler, D. S. Boyd, G. M. Foody, and A. Vetrivel, "Estimating tropical forest biomass with a combination of SAR image texture and Landsat TM data: An assessment of predictions between regions," *ISPRS J. Photogrammetry Remote Sens.*, vol. 70, pp. 66–77, 2012.

[37] J. Chang and M. Shoshany, "Mediterranean shrublands biomass estimation using sentinel-1 and Sentinel-2," in *Proc. Int. Geosci. Remote Sens. Symp.*, 2016, pp. 5300–5303.

[38] J. Lei, X. Song, L. Sun, M. Song, N. Li, and C. Chen, "Learning deep classifiers with deep features," in *Proc. - IEEE Int. Conf. Multimedia Expo.*, 2016, pp. 2–7.

[39] X. Y. Tong, G. S. Xia, F. Hu, Y. Zhong, M. Datcu, and L. Zhang, "Exploiting deep features for remote sensing image retrieval: A systematic investigation," *IEEE Trans. Big Data*, vol. 6, no. 3, pp. 507–521, Sep. 2020.

[40] L. Xu, Y. Chen, S. Srinivasan, N. de Freitas, A. Doucet, and A. Gretton, "Learning deep features in instrumental variable regression," in *Proc. 9th Int. Conf. Learn. Representations*, Virtual Event, Austria, 2021, doi: 10.48550/ARXIV.2010.07154.

[41] N. T. Ha, M. Manley-Harris, T. D. Pham, and I. Hawes, "The use of radar and optical satellite imagery combined with advanced machine learning and metaheuristic optimization techniques to detect and quantify above ground biomass of intertidal seagrass in a New Zealand estuary," *Int. J. Remote Sens.*, vol. 42, no. 12, pp. 4716–4742, 2021.

[42] S. Vafaei *et al.*, "Improving accuracy estimation of forest aboveground biomass based on incorporation of ALOS-2 PALSAR-2 and Sentinel-2A imagery and machine learning: A case study of the Hyrcanian forest area (Iran)," *Remote Sens.,* vol. 10, no. 2, p. 172, 2018.

[43] H. Su, W. Shen, J. Wang, A. Ali, and M. Li, "Machine learning and geostatistical approaches for estimating aboveground biomass in Chinese subtropical forests," *Forest Ecosyst.*, vol. 7, no. 1, pp. 1–20, Dec. 2020.
[44] R. C. Sharma, "Ensemble learning of multi-source satellite sensors dataset for estimating forest biomass in New England region," *MDPI Preprint*, 2021, Art. no. 2021020338, doi: 10.20944/preprints202102.0338.v1.
[45] X. Li, M. Zhang, J. Long, and H. Lin, "A novel method for estimating spatial distribution of forest above-ground biomass based on multispectral fusion data and ensemble learning algorithm," *Remote Sens.,* vol. 13, no. 19, 2021, Art. no. 3910.
[46] X. X. Zhu *et al.*, "Deep learning in remote sensing: A review," *IEEE Geosci. Remote Sens. Mag.*, vol. 5, no. 4, pp. 8–36, Dec. 2017.
[47] L. Ma, Y. Liu, X. Zhang, Y. Ye, G. Yin, and B. A. Johnson, "Deep learning in remote sensing applications: A meta-analysis and review," *ISPRS J. Photogrammetry Remote Sens.*, vol. 152, pp. 166–177, 2019.
[48] G. Tsagkatakis, A. Aidini, K. Fotiadou, M. Giannopoulos, A. Pentari, and P. Tsakalides, "Survey of deep-learning approaches for remote sensing observation enhancement," *Sensors (Switzerland)*, vol. 19, no. 18, 2019, Art. no. 3929.
[49] A. Romero, C. Gatta, and G. Camps-Valls, "Unsupervised deep feature extraction for remote sensing image classification," *IEEE Trans. Geosci. Remote Sens.*, vol. 54, no. 3, pp. 1349–1362, Mar. 2016.
[50] S. Ghosh, L. Bruzzone, S. Patra, F. Bovolo, and A. Ghosh, "A context-sensitive technique for unsupervised change detection based on hopfield-type neural networks," *IEEE Trans. Geosci. Remote Sens.*, vol. 45, no. 3, pp. 778–788, Mar. 2007.
[51] J. E. Ball, D. T. Anderson, and C. S. Chan, "Comprehensive survey of deep learning in remote sensing: Theories, tools, and challenges for the community," *J. Appl. Remote Sens.*, vol. 11, no. 4, 2017, Art. no. 042609.
[52] M. Zhu, Y. He, and Q. He, "A review of researches on deep learning in remote sensing application," *Int. J. Geosci.*, vol. 10, no. 1, pp. 1–11, 2019.
[53] T. Hoeser, F. Bachofer, and C. Kuenzer, "Object detection and image segmentation with deep learning on earth observation data: A review-part II: Applications," *Remote Sens.,* vol. 12, no. 18, p. 3053, 2020.
[54] L. Zhu, Y. Chen, P. Ghamisi, and J. A. Benediktsson, "Generative adversarial networks for hyperspectral image classification," *IEEE Trans. Geosci. Remote Sens.*, vol. 56, no. 9, pp. 5046–5063, Sep. 2018.
[55] X. Liu, Y. Wang, and Q. Liu, "Psgan: A generative adversarial network for remote sensing image pan-sharpening," *Proc. - Int. Conf. Image Process.*, vol. 14, no. 8, pp. 873–877, 2018.
[56] V. Betina, "(Improved PPF)Going further with point pair features," *Neoplasma*, vol. 16, no. 1, pp. 23–32, 2016.
[57] Z. Wang, Q. She, and T. E. Ward, "Generative adversarial networks in computer vision: A survey and taxonomy," *ACM Comput. Surv.*, vol. 54, no. 2, pp. 1–41, 2021.
[58] C. Li, K. Xu, J. Zhu, and B. Zhang, "Triple generative adversarial nets," *Adv. Neural Inf. Process. Syst.*, vol. 2017, pp. 4089–4099, 2017.
[59] B. Rodríguez-Suárez, P. Quesada-Barriuso, and F. Argüello, "Design of CGAN models for multispectral reconstruction in remote sensing," *Remote Sens.*, vol. 14, no. 4, p. 816, Feb. 2022, doi: 10.3390/rs14040816.
[60] Y. Yoo, S. Yun, H. J. Chang, Y. Demiris, and J. Y. Choi, "Variational autoencoded regression: High dimensional regression of visual data on complex manifold," in *Proc. 30th IEEE Conf. Comput. Vis. Pattern Recognit.*, 2017, pp. 2943–2952.
[61] X. Li *et al.*, "Learning disentangled feature representation for hybrid-distorted image restoration," *Lecture Notes Comput. Sci. (Including Subseries Lecture Notes Artif. Intell. Lecture Notes Bioinf.)*, vol. 12374, pp. 313–329, 2020.
[62] Y. Liu, F. Wei, J. Shao, L. Sheng, J. Yan, and X. Wang, "Exploring disentangled feature representation beyond face identification," in *Proc. IEEE Comput. Soc. Conf. Comput. Vis. Pattern Recognit.*, 2018, pp. 2080–2089.
[63] C. T. Marx, R. L. Phillips, S. A. Friedler, C. Scheidegger, and S. Venkatasubramanian, "Disentangling influence: Using disentangled representations to audit model predictions," *Adv. Neural Inf. Process. Syst.*, vol. 32, pp. 1–11, 2019.
[64] A. H. Liu, Y. C. Liu, Y. Y. Yeh, and Y. C. F. Wang, "A unified feature disentangler for multi-domain image translation and manipulation," *Adv. Neural Inf. Process. Syst.*, vol. 2018, pp. 2590–2599, 2018.
[65] F. Del Frate and D. Solimini, "On neural network algorithms for retrieving forest biomass from SAR data," *IEEE Trans. Geosci. Remote Sens.*, vol. 42, no. 1, pp. 24–34, Jan. 2004.
[66] L. Zhang, Z. Shao, J. Liu, and Q. Cheng, "Deep learning based retrieval of forest aboveground biomass from combined LiDAR and landsat 8 data," *Remote Sens.,* vol. 11, no. 12, 2019, Art. no. 1459.
[67] Z. Shao, L. Zhang, and L. Wang, "Stacked sparse autoencoder modeling using the synergy of airborne LiDAR and satellite optical and SAR data to map forest above-ground biomass," *IEEE J. Sel. Topics Appl. Earth Observ. Remote Sens.*, vol. 10, no. 12, pp. 5569–5582, Dec. 2017.
[68] M. Dalponte and D. A. Coomes, "Tree-centric mapping of forest carbon density from airborne laser scanning and hyperspectral data," *Methods Ecol. Evol.*, vol. 7, no. 10, pp. 1236–1245, 2016.
[69] J. Louis *et al.*, "Sentinel-2 SEN2COR: L2A processor for users," in *Proc. Living Planet Symp.*, 2016, pp. 1–8.
[70] N. Bhogapurapu, S. Dey, D. Mandal, A. Bhattacharya, and Y. Rao, "PolSAR tools: A QGIS plugin for generating SAR descriptors," *J. Open Source Softw.*, vol. 6, no. 60, 2021, Art. no. 2970.
[71] T. D. Nguyen and M. Kappas, "Estimating the aboveground biomass of an evergreen broadleaf forest in Xuan Lien Nature Reserve, Thanh Hoa, Vietnam, using SPOT-6 data and the random forest algorithm," *Int. J. Forestry Res.*, vol. 2020, pp. 1–13, Aug. 2020, doi: 10.1155/2020/4216160.
[72] C. Wu *et al.*, "Comparison of machine-learning methods for above-ground biomass estimation based on Landsat imagery," *J. Appl. Remote Sens.*, vol. 10, no. 3, 2016, Art. no. 035010.
[73] Y. Zhang, J. Ma, S. Liang, X. Li, and M. Li, "An evaluation of eight machine learning regression algorithms for forest aboveground biomass estimation from multiple satellite data products," *Remote Sens.*, vol. 12, no. 24, 2020, Art. no. 4015.
[74] G. Scrinzi, D. Galvagni, and L. Marzullo, *I Nuovi Modelli Dendrometrici per La Stima Delle Masse Assestamentali in Provincia di Trento*. Trento, Italy: Provincia Autonoma di Trento-Servizio Foreste e fauna, 2010.
[75] IPCC, "Good practice guidance for land use, land-use change and forestry," in *Proc. Nat. Greenhouse Gas Inventories Prog.*, Kanagawa, Japan, 2013, pp. 1.1–5.76.
[76] N. Hayatbini *et al.*, "Conditional generative adversarial networks (cGANs) for near real-time precipitation estimation from multispectral GOES-16 satellite imageries-PERSIANN-cGAN," *Remote Sens.*, vol. 11, no. 19, 2019, Art. no. 2193.